# Full-Time Monocular Road Detection Using Zero-Distribution Prior of Angle of Polarization

# Supplementary Material

Ning Li[1], Yongqiang Zhao[1], Quan Pan[1], Seong G. Kong[2], and Jonathan Cheung-Wai Chan[3]

[1] Northwestern Polytechnical University, Xi'an, 710072, China
[2] Sejong University, Seoul, 05006, South Korea
[3] Vrije Universiteit Brussel, Brussel, 1050, Belgium

This supplementary material contains the following details that we could not include in the main paper due to space restrictions. Sec. 1: Background introduction of DoFP polarization imaging and Stokes parameters. Sec. 2: Detailed proof of sign of $S_1$. Sec. 3: Statistical analysis of difference of DoP. Sec. 4: More experiment results.

## 1 Background

A polarization imaging system collects polarization information in different orientations. Various types of existing polarization imagers include division of time, division of amplitude, division of aperture, and division of focal plane (DoFP) [8]. DoFP polarimeter has received much attention due to its integrated sample structure and the ability of capturing polarization information in real time. DoFP polarimeters capture images using a micro-polarizer array (MPA) image sensor as shown in Fig. 1. Each pixel takes the polarized light at only one of four orientations, e.g. 0, 45, 90, and 135 degrees. Missing polarization components at neighboring pixels need to be estimated, or interpolated, since the instantaneous field of view (IFoV) [5] errors will become significant. This polarization interpolation process is called polarization demosaicking (PDM). So, it generates four polarization images after the PDM on the input DoFP image.

A DoFP polarimeter with the structure in Fig. 1 to capture intensity and polarization information of a scene is essentially an intensity-based method. The four recovered full resolution intensity measurements $I_\phi(x)$ (the light wave filtered by micro linear polarizer oriented at $\phi = 0°, 45°, 90°, 135°$) after PDM are necessary and sufficient to compute the polarization parameters as follows [4]

$$\begin{aligned} S_0(x) &= 0.5\,(I_0(x) + I_{45}(x) + I_{90}(x) + I_{135}(x)) \\ S_1(x) &= I_0(x) - I_{90}(x) \\ S_2(x) &= I_{45}(x) - I_{135}(x) \end{aligned} \tag{1}$$

where $S_0$, $S_1$ and $S_2$ are known as the first three Stokes parameters, and $x$ is pixel position. $S_0$ is the total intensity of the light. The parameters $S_1$ and $S_2$

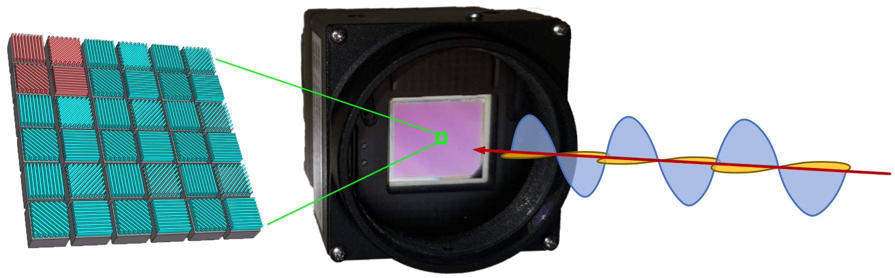

**Fig. 1.** A DoFP infrared polarization imaging system with a micro-polarizer array

describe the amount of linear polarization. To observe polarization, two polarization properties are of most interest, degree of linear polarization (DoP) $D(x)$ and angle of polarization (AoP) $A(x)$, defined as [10]

$$\begin{aligned} D(x) &= \frac{\sqrt{S_1(x)^2+S_2(x)^2}}{S_0(x)} \\ A(x) &= \frac{1}{2}\tan^{-1}\left(\frac{S_2(x)}{S_1(x)}\right) \end{aligned} \tag{2}$$

The Stokes parameter $S_3$ that describes circular polarization is not captured with the DoFP imager as shown in Fig. 1 for lack of retarder. In fact, the measurements with four linear polarization filters offset by 45° are optimal for maximization of signal-to-noise ratio and minimization of systematic error [6], [7].

## 2 Proof: Sign of $S_1$

The thermal radiation reaches the DoFP LWIR detector contains the reflected radiation $R$ and emitted radiation $E$, and both are expressed as the sum of two orthogonal polarized components, that is, $R = R_{\parallel} + R_{\perp}$ and $E = E_{\parallel} + E_{\perp}$. Fig. 2 shows the geometry of how the thermal radiation captured by detector is formed.

For an unpolarized incident radiation with unit emissivity of temperature $T_0$, total p-polarized radiance and s-polarized radiance leaving the road surface with complex index of refraction $n' = n + k\mathrm{i}$ at temperature $T_1$ in direction $\theta$ [9] are given as

$$L_{\parallel}(\theta, n') = R_{\parallel} + E_{\parallel} = P\left(T_0\right) r_{\parallel}(\theta, n') + P\left(T_1\right) \varepsilon_{\parallel}(\theta, n') \tag{3}$$

$$L_{\perp}(\theta, n') = R_{\perp} + E_{\perp} = P\left(T_0\right) r_{\perp}(\theta, n') + P\left(T_1\right) \varepsilon_{\perp}(\theta, n') \tag{4}$$

where $P\left(T\right)$ denotes the Planck Blackbody radiance curve at temperature $T$, $\varepsilon$ is the emissivity and $r$ is the reflectivity in the p- and s-polarization states. The special subscripts $\parallel$ and $\perp$ are added to $\varepsilon$ and $r$ that correspond to respectively the polarized components parallel and perpendicular to the plane of incidence.

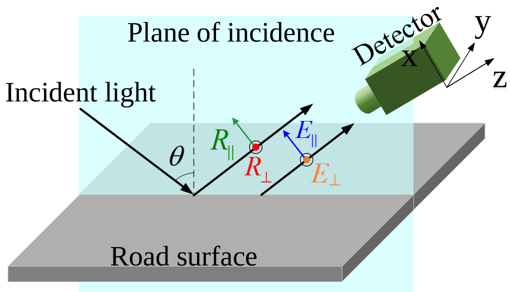


**Fig. 2.** Mode of how the thermal radiation capture by detector is formed in LWIR and we consider the measured polarization signatures are primarily due to emissions from the road surface

In Eqs. (3) and (4), we assume that the emissivity and reflectivity are spectrally flat over the wavelength range of interest, which is a reasonable assumption when working in the LWIR. For road surface, the measured polarization signatures are primarily due to emissions from the surface, where $T_0 \ll T_1$. Eqs (3) and (4) can be rewritten as

$$L_{\parallel}(\theta, n') \approx E_{\parallel} = P\left(T_1\right) \varepsilon_{\parallel}(\theta, n') \tag{5}$$

$$L_{\perp}(\theta, n') \approx E_{\perp} = P\left(T_1\right) \varepsilon_{\perp}(\theta, n') \tag{6}$$

According to [1], for a smooth opaque material with complex index of refraction $n'$, the directional emissivity is given by Fresnel's equations

$$\varepsilon_v\left(\theta, n'\right) = \frac{2}{1+z_v} \quad (v = \perp, \parallel) \tag{7}$$

where

$$\begin{aligned} z_\perp &= \frac{c+\cos^2\theta}{\sqrt{2}\cos\theta\left(c+a-\sin^2\theta\right)^{\frac{1}{2}}} \\ z_\parallel &= \frac{c+\left(a^2+b^2\right)\cos^2\theta}{\sqrt{2}\cos\theta\left[c\left(a^2+b^2\right)+\left(a-\sin^2\theta\right)\left(a^2-b^2\right)+2ab^2\right]^{\frac{1}{2}}} \end{aligned} \tag{8}$$

$z$ is defined by $a$, $b$, $c$ and $n'$, whose definitions are:

$$\begin{aligned} a &= \mathrm{Re}\left(\left(n'\right)^2\right) \\ b &= \mathrm{Im}\left(\left(n'\right)^2\right) \\ c &= \sqrt{\left(a-\sin^2\theta\right)^2+b^2} \end{aligned} \tag{9}$$

Since a light vector can be decomposed into two orthogonal components [4], we only consider the emission light that propagates along the observation direction from the road since the emitted radiation dominates. In the coordinate

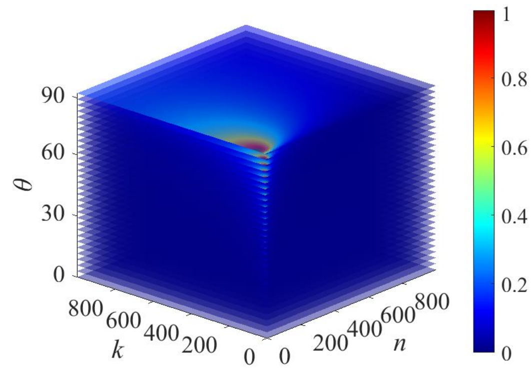


**Fig. 3.** $\varepsilon_{\|}(\theta, n')^2 - \varepsilon_{\perp}(\theta, n')^2$ vary with respect to $\theta$, $n$ and $k$

system in Fig. 2, the transverse components are parallel and perpendicular to the plane of incidence in terms of complex notation

$$E_x(t) = E_{0x} \exp\left[i\left(\omega t + \delta_x\right)\right] \tag{10}$$

$$E_y(t) = E_{0y} \exp\left[i\left(\omega t + \delta_y\right)\right] \tag{11}$$

where $E_{0x}$ and $E_{0y}$ are the amplitudes, and $\delta_x$ and $\delta_y$ are the phases, respectively. According to Eqs. (5) and (6), we have

$$E_{0x} = E_{\|} = P\left(T_1\right) \varepsilon_{\|}(\theta, n') \tag{12}$$

$$E_{0y} = E_{\perp} = P\left(T_1\right) \varepsilon_{\perp}(\theta, n') \tag{13}$$

The Stokes parameter $S_1$ for the emitted field is [4]

$$S_1 = n \cos\theta \left(E_x E_x^* - E_y E_y^*\right) \tag{14}$$

Substituting Eqs. (10) and (11) into Eq. (14) gives

$$\begin{aligned} S_1 &= n \cos\theta \left(E_{0x}^2 - E_{0y}^2\right) = n \cos\theta \left(E_{\|}^2 - E_{\perp}^2\right) \\ &= n \cos\theta \cdot P\left(T_1\right)^2 \cdot \left(\varepsilon_{\|}(\theta, n')^2 - \varepsilon_{\perp}(\theta, n')^2\right) \end{aligned} \tag{15}$$

Since $n > 0$ and $\cos\theta > 0$ ($\theta \in (0, 90°)$), the sign of $S_1$ is decided by the sign of $\varepsilon_{\|}(\theta, n')^2 - \varepsilon_{\perp}(\theta, n')^2$ and it is decided by incident angle $\theta$, real part $n$ and imaginary part $k$ of the complex index of refraction $n'$ of road. Since the exact refraction $n'$ of the road is unknown, the intervals are set to $n \in (0, 1000]$ and $k \in (0, 1000]$. We calculate the value of $\varepsilon_{\|}(\theta, n')^2 - \varepsilon_{\perp}(\theta, n')^2$ and plot the result with $\theta$, $n$ and $k$ in Fig. 3. The quantity $\varepsilon_{\|}(\theta, n')^2 - \varepsilon_{\perp}(\theta, n')^2$ is positive in a sufficiently large interval, so $S_1$ is also positive.

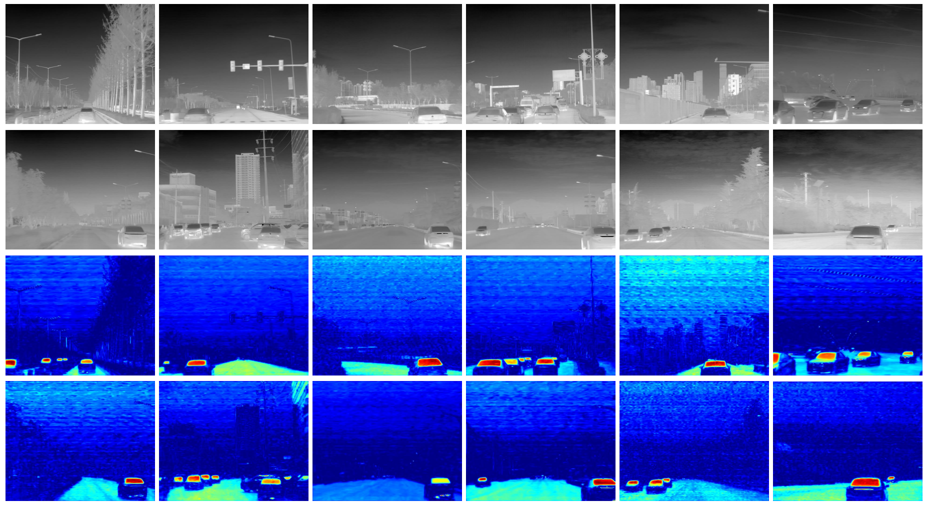

**Fig. 4.** Top: example images in our DoFP road scene database. Bottom: the corresponding DoP images

## 3 Difference of DoP

Another important task in road detection is to separate vehicles from the road. Based on the analysis in Section 3 in main paper, the hood and windshield have similar AoP with road. Therefore, cars can be misclassified as the road if we only use the zero-distribution prior. Fig. 4 shows several road scenes and the corresponding DoP images in pseudo color. We find that there are regular differences between road and vehicles, that is the DoP of hood and windshield are usually higher and DoP of other parts (like the front, back and left or right side) of the vehicle are always lower than that of road, which agrees with the observation in former researches [2], [3] of vehicle detection. We call this characteristic of DoP of vehicle and road the *difference of DoP*.

We select 200 images with different number of vehicles and make a statistical analysis of the distribution of DoP of road and vehicle. In practice, DoP of different road scenes may have different distribution range. Since direct statistical analysis with the original DoP image is unavailable, we first normalize the original DoP image by

$$D_N(x) = \begin{cases} 0.5\frac{D_o(x)-D_{\min}}{\bar{D}_r-D_{\min}} & , D_o(x) < \bar{D}_r \\ 0.5\left(\frac{D_o(x)-\bar{D}_r}{D_{\max}-\bar{D}_r}+1\right) & , D_o(x) \geq \bar{D}_r \end{cases} \tag{16}$$

where $D_N(x)$ is normalized DoP and $D_o(x)$ is original DoP, $D_{\max}$ and $D_{\min}$ represent the maximum and minimum DoP in road and vehicle region respectively, and $\bar{D}_r$ is the average DoP in road region. Therefore, the normalized DoP images are in the same range. We can make a statistical analysis of total 200 selected images. Fig. 5 shows that clear differences of DoP exist between road and

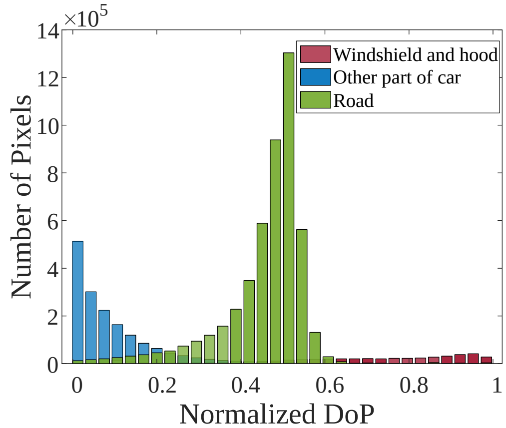


**Fig. 5.** Histogram of range normalized DoP in road and different part of vehicle regions of 200 selected road scenes

vehicle. This characteristic helps separate the vehicle and road. The normalized DoP images are only used for statistical analysis, and we still use original DoP images for road segmentation.

## 4 Additional Results

**Horizon detection**. For horizon detection, Fig. 6 shows more results under several different road scenes, including the curve road, road gets blocked or road goes up. And the proposed horizon detection method is efficient and robust under those different road situations.

One may concern that what if there is no horizon exists or its hard to detect horizon under the difficult road scenes like road goes uphill or gets blocked and so on. In such cases the horizon detection may not be as accurate as other normal road scenes, but this won't affect the final results of the joint road detection as the frame of the proposed methodology doesn't rely heavily on horizon detection accuracy. The horizon is mainly used for reducing the computation load and the interference from the upper part of the image. As shown in Fig. 7, the horizon detection is not that accurate under several difficult road situations, but the final road detection results are still gratifying.

**Road detection**. Here we provide more road detection results under different road scenes at both day time and night time. Fig. 8 shows the road detection results at day time and Fig. 9 shows the road detection results at night time. We also provide several road detection video clips at https://youtu.be/axmkPoFW234.

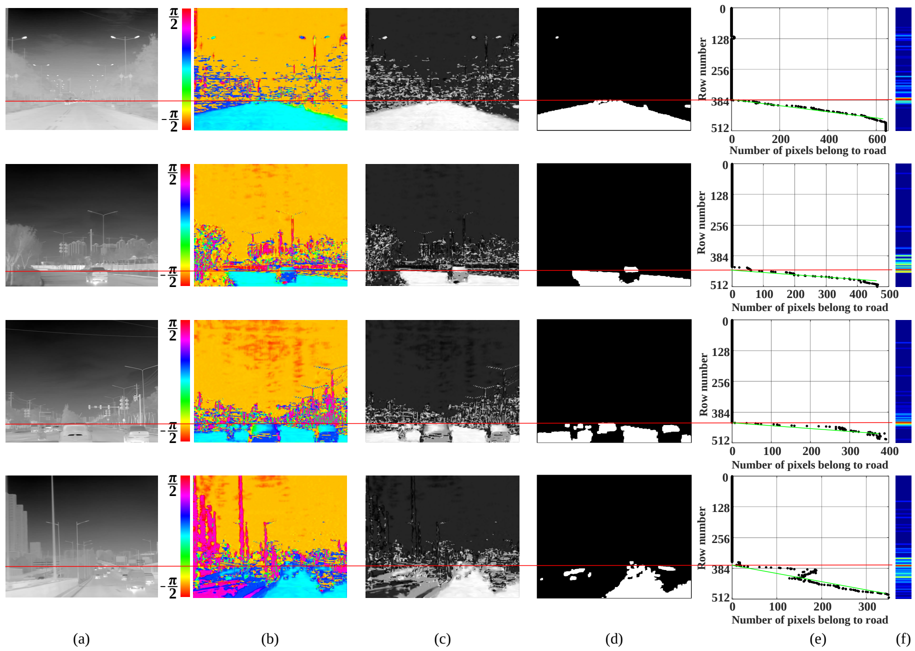


**Fig. 6.** Examples for horizon detection. (a) Input DoFP image, (b) AoP image, (c) coarse road estimation, (d) coarse road map, (e) 1D projection of the coarse road map, (f) piecewise cumulative energy of horizon confidence map

## References

1. Ben-Dor, B., Oppenheim, U.P., Balfour, L.S.: Polarization properties of targets and backgrounds in the infrared. In: 8th Meeting on Optical Engineering in Israel: Optical Engineering and Remote Sensing. vol. 1971, pp. 68–77. International Society for Optics and Photonics (1993)
2. Dickson, C.N., Wallace, A.M., Kitchin, M., Connor, B.: Long-wave infrared polarimetric cluster-based vehicle detection. JOSA A **32**(12), 2307–2315 (2015)
3. Dickson, C., Wallace, A.M., Kitchin, M., Connor, B.: Improving infrared vehicle detection with polarisation (2013)
4. Goldstein, D.H.: Polarized light. CRC press (2016)
5. Ratliff, B.M., LaCasse, C.F., Tyo, J.S.: Interpolation strategies for reducing ifov artifacts in microgrid polarimeter imagery. Optics express **17**(11), 9112–9125 (2009)
6. Tyo, J.S.: Optimum linear combination strategy for an n-channel polarization-sensitive imaging or vision system. JOSA A **15**(2), 359–366 (1998)
7. Tyo, J.S.: Design of optimal polarimeters: maximization of signal-to-noise ratio and minimization of systematic error. Applied optics **41**(4), 619–630 (2002)
8. Tyo, J.S., Goldstein, D.L., Chenault, D.B., Shaw, J.A.: Review of passive imaging polarimetry for remote sensing applications. Applied Optics **45**(22), 5453–5469 (2006)

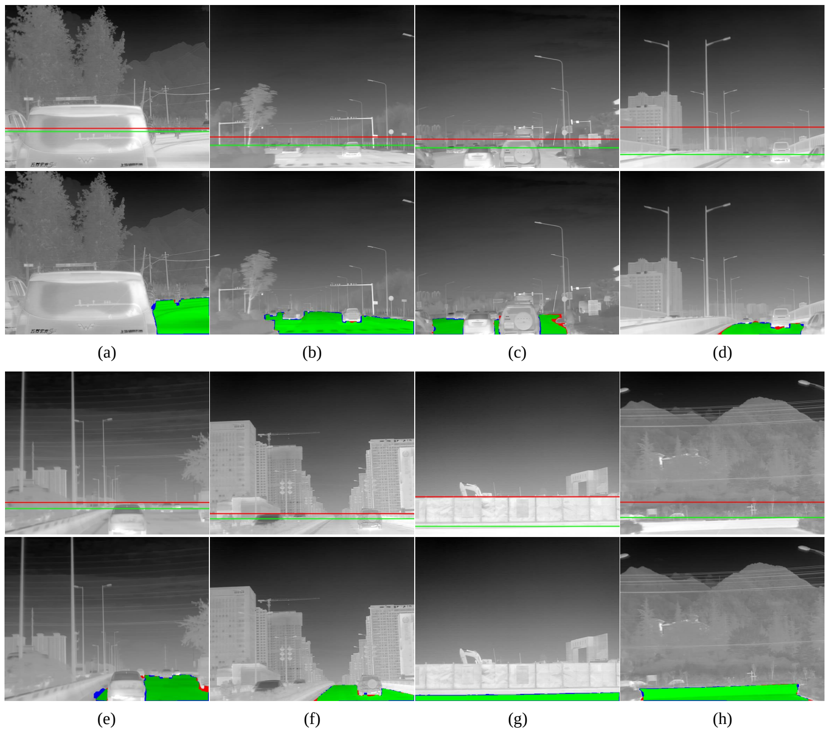


**Fig. 7.** Road detection results under the situations where the horizon detection is not as accurate as other normal road scenes or there is even no horizon exists. For each group of results, the top is the horizon detection result and the bottom is the corresponding road detection result based on the proposed method. Note that the green line is the ground-truth horizon and the red line is the detected horizon. And green region corresponds to true positive, red region represents false negative and blue region denotes false positive. (a)-(c) Road regions get blocked or are irregular. (d)-(f) Roads go up where no horizon exists. (g)-(h) It's a dead end where the road ahead

9. Tyo, J.S., Ratliff, B.M., Boger, J.K., Black, W.T., Bowers, D.L., Fetrow, M.P.: The effects of thermal equilibrium and contrast in lwir polarimetric images. Optics express **15**(23), 15161–15167 (2007)
10. Zhao, Y., Yi, C., Kong, S.G., Pan, Q., Cheng, Y.: Multi-band polarization imaging. In: Multi-band Polarization Imaging and Applications, pp. 47–71. Springer (2016)

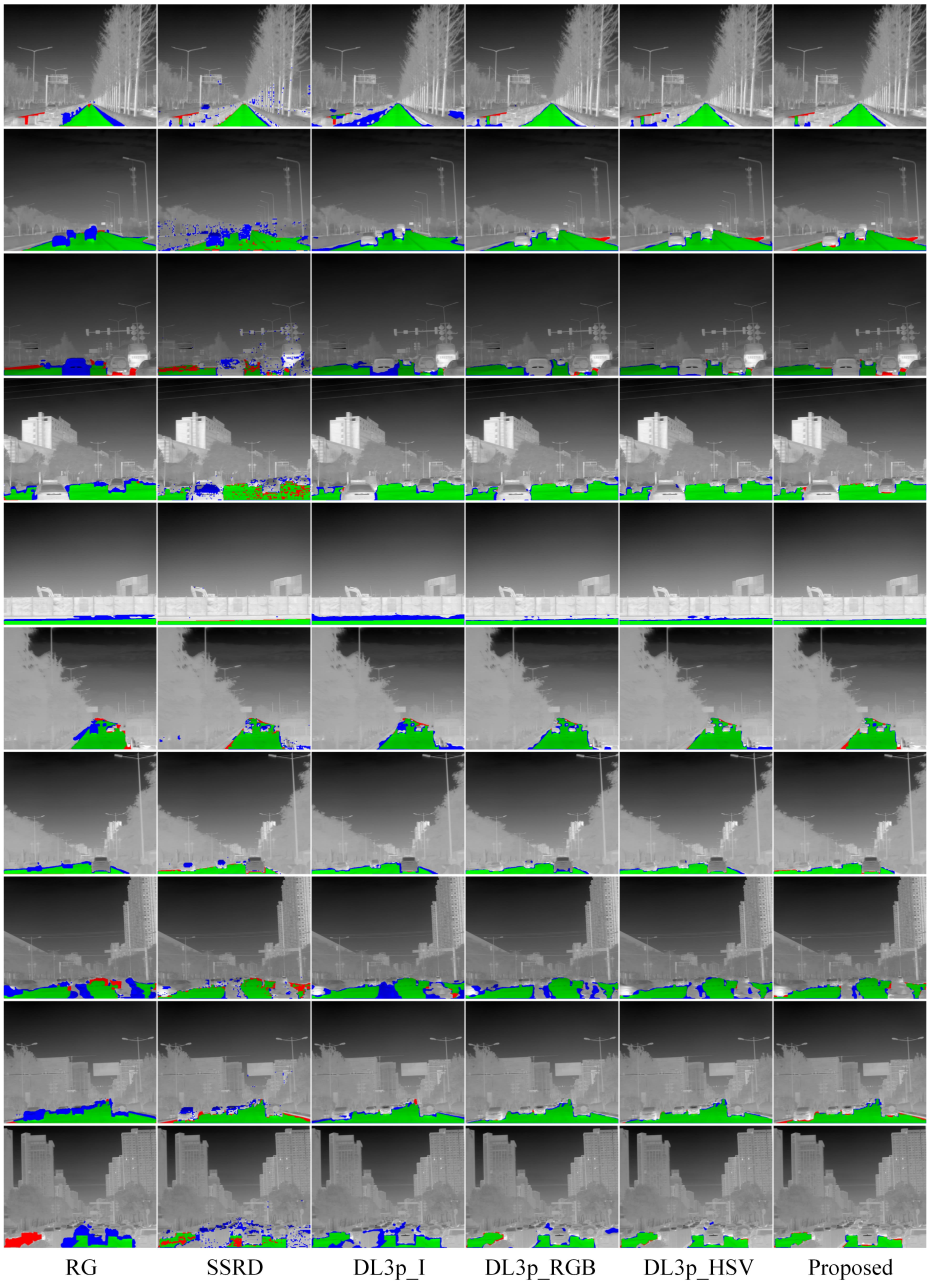


**Fig. 8.** Road detection results of different methods at day time, and green region corresponds to true positive, red region represents false negative and blue region denotes false positive

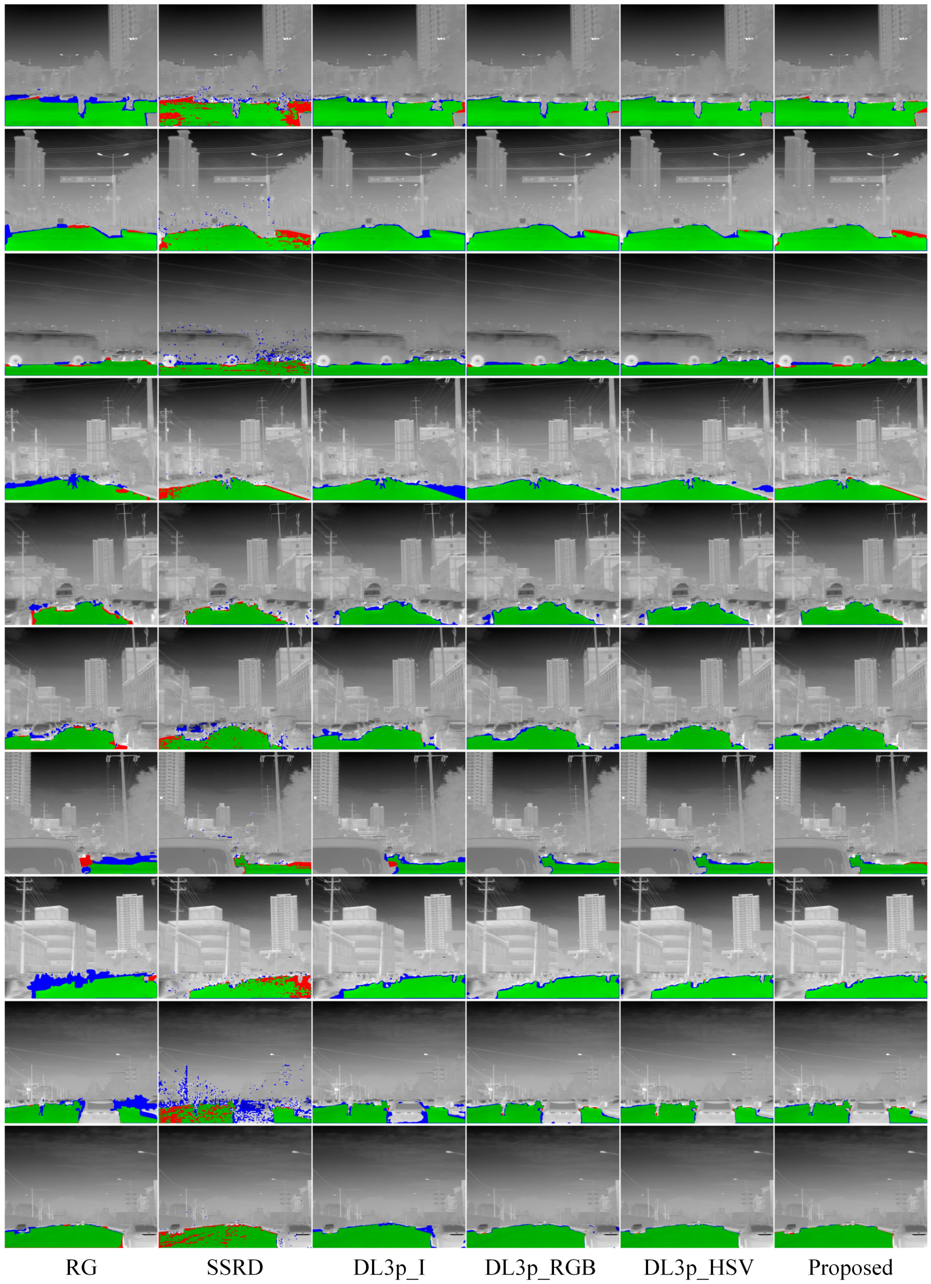


**Fig. 9.** Road detection results of different methods at night time, and green region corresponds to true positive, red region represents false negative and blue region denotes false positive